Iowa State University

From the SelectedWorks of Mark S. Gordon

June, 1989

Ab Initio Reaction Paths and Direct Dynamics Calculations

Kim K. Baldridge
Mark S. Gordon
Rozeanne Steckler, *University of Minnesota - Twin Cities*
Donald G. Truhlar, *University of Minnesota - Twin Cities*

Available at: https://works.bepress.com/mark_gordon/86/

the hydrogen of an acid such as HF approaches the peripheral of the benzene ring along an axis tilted toward the ring axis as predicted by the properties of the Laplacian distribution,[1] to form a weak π complex. In this complex, the bond path from the proton flicks from a carbon atom to a C–C bond with essentially no change in energy. The transformation of the complex into the protonated intermediate involves the charge rearrangements described above, and these are different from the pattern of charges found in the reactant molecules that determine the initial site of attack, and they involve much greater changes in the energy.

Acknowledgment. Acknowledgment is made to the donors of the Petroleum Research Fund, administered by the American Chemical Society, for partial support of this research.

Appendix

Table AI summarizes the manner in which the substituents O^-, NH_2, OH, F, CH_3, CN, and NO_2 perturb the atomic populations of the benzene ring. The optimized geometries and corresponding energies of the protonated intermediates and protonated benzene, determined with basis sets 3-21G, 4-31G, 6-31G, and 6-31G*, are tabulated in Tables AII–AVI.

Registry No. [PhH]H^+, 26812-57-7; [*p*-PhOH]H^+, 53280-65-2; [*m*-PhOH]H^+, 83608-47-3; [*p*-PhF]H^+, 57525-23-2; [*m*-PhF]H^+, 74309-51-6; [*p*-PhCN]H^+, 87176-59-8; [*m*-PhCN]H^+, 87176-58-7; $(CH_3)_2CHCH(CH_3)C^+(CH_3)CH(CH_3)CH(CH_3)_2$, 120497-33-8; phenol, 108-95-2; fluorobenzene, 462-06-6; benzene, 71-43-2; benzonitrile, 100-47-0.

Ab Initio Reaction Paths and Direct Dynamics Calculations

Kim K. Baldridge, Mark S. Gordon,*

Department of Chemistry, North Dakota State University, Fargo, North Dakota 58105

Rozeanne Steckler, and Donald G. Truhlar*

Department of Chemistry and Supercomputer Institute, University of Minnesota, Minneapolis, Minnesota 55455 *(Received: November 8, 1988; In Final Form: January 20, 1989)*

A detailed study of methods for generating the minimum energy path of a chemical reaction using ab initio electronic structure calculations is presented; the convergence with respect to step size of the geometry and energy along this path is studied with several algorithms. The investigations are extended to the calculation of chemical reaction rate coefficients by interfacing the POLYRATE code for variational transition-state theory and semiclassical tunneling calculations with a locally modified GAUSSIAN82 electronic structure package that now contains reaction path following capabilities at both the Hartree–Fock and perturbation theory levels. This combined package is used to study the kinetics of the abstraction reaction $CH_3 + H_2 \rightarrow CH_4 + H$, which is considered as a prototype organic reaction. We report calculations of reaction rates based on electronic structure theory and generalized transition-state theory, including a multidimensional tunneling correction, without performing an analytic fit to the potential surface. The calculation of dynamical processes directly from ab initio electronic structure input without the intermediary of a potential surface fit is called "direct dynamics", and this paper demonstrates the feasibility of this approach for bimolecular reactions.

1. Introduction

The prediction of rate constants by ab initio methods is limited by the computational effort of calculating and fitting reactive potential energy surfaces (PESs). The advances[1] made in the calculation of energy gradients and higher order derivatives of potential surfaces have, however, been an important factor in reducing this effort, in particular by allowing the potential to be calculated efficiently along a reaction path. This in turn raises the question of the accuracy with which the minimum energy path (MEP) for a reaction must be calculated in order to obtain a reaction path representation well-enough converged to calculate accurate thermal rate constants. Standard two-point and higher order methods for integrating differential equations and simple specialized methodologies have been tested in this context with regard to the step size taken along the reaction path, which must be balanced against computer time constraints.[2-4] The work presented herein provides an extension of these investigations. Additional methods are tested, and we report a complete calculation of a bimolecular reaction rate based directly on an ab initio reaction path, its curvature, and a harmonic approximation to the potential orthogonal to it—without the intermediate step of fitting the potential energy surface.

There are two important reasons for investigating sophisticated techniques for tracing the MEP. First, the equations for the minimum energy path may be governed by a "stiff" set of differential equations for some chemical systems. Standard numerical techniques may fail when applied to stiff systems of differential equations, or they may require an extremely small step size; alternatively, one may apply numerical techniques especially designed for stiff systems.[5,6] Second, even when the equations

(1) (a) Pulay, P. In *Applications of Electronic Structure Theory*; Schaefer, H. F., Ed.; Plenum Press: New York, 1977; p 153. (b) Pople, J. A.; Krishnan, R. A.; Schlegel, H. B. *Int. J. Quantum Chem., Quantum Chem. Symp.* **1979**, *No. 13*, 225. (c) Morokuma, K.; Kato, S. In *Potential Energy Surfaces and Dynamics Calculations*; Truhlar, D. G., Ed.; Plenum Press: New York, 1981; p 243. (d) Morokuma, K.; Kato, S.; Kitaura, K.; Ubara, S.; Ohta, K.; Hanamura, M. In *New Horizons in Quantum Chemistry*; Löwdin, P.-O., Pullman, B., Eds.; Reidel: Dordrecht, The Netherlands, 1983; p 221. (e) Gaw, J. F.; Yamaguchi, Y.; Schaefer, H. F. *J. Chem. Phys.* **1984**, *81*, 6395.

(2) Schmidt, M. W.; Gordon, M. S.; Dupuis, M. J. *J. Am. Chem. Soc.* **1985**, *107*, 2585.

(3) Truhlar, D. G.; Brown, F. B.; Steckler, R.; Isaacson, A. D. In *The Theory of Chemical Reaction Dynamics*; Clary, D., Ed.; Reidel: Dordrecth, The Netherlands, 1986; p 285.

(4) Garrett, B. C.; Redmon, M. J.; Steckler, R.; Truhlar, D. G.; Baldridge, K. K.; Bartol, D.; Schmidt, M. W.; Gordon, M. S. *J. Phys. Chem.* **1988**, *92*, 1476.

(5) (a) Curtiss, C. F.; Hirschfelder, J. O. *Proc. Natl. Acad. Sci. U.S.A.* **1952**, *38*, 235. (b) Butcher, J. *Math. Computation* **1965**, *19*, 408. (c) Davis, P. J.; Polonsky, I. In *Handbook of Mathematical Functions*; Abramowitz, M., Stegun, I. A., Eds.; National Bureau of Standards: Washington, DC, 1964; p 875. (d) Carnahan, B.; Luther, H. A.; Wilkes, J. O. *Applied Numerical Methods*; Wiley: New York, 1969. (e) Gear, C. W. *Numerical Initial Value Problems in Ordinary Differential Equations*; Prentice-Hall: New Jersey, 1971. (f) Miller, W. H.; George, T. F. *J. Chem. Phys.* **1972**, *56*, 5668. (g) Hildebrand, F. B. *Introduction to Numerical Analysis*, 2nd ed., McGraw-Hill: New York, 1974. (h) Burden, R. L.; Faires, J. D.; Reynolds, A. C. *Numerical Analysis*; Prindle, Weber, and Schmidt: Boston, 1978. (i) Shampine, L. F.; Gear, C. W. *SIAM Rev.* **1979**, *21*, 1. (j) Stoer, J.; Bulirsch, R. *Introduction to Numerical Analysis*; Springer-Verlag: New York, 1980. (k) Gupta, G. K.; Sacks-Davis, R.; Tischer, P. E. *Computing Surveys* **1985**, *17*, 10. (l) Press, W. H.; Flannery, B. P.; Tevkolsky, S. A.; Vetterling, W. T. *Numerical Recipies: The Art of Scientific Computing*; Cambridge University Press: New York, 1986. (m) Strang, G. *Introduction to Applied Mathematics*; Wellesley-Cambridge Press: Wellesley, MA, 1986. (n) Byrne, G. D.; Hindmarsh, A. C. *J. Comput. Phys.* **1987**, *70*, 1.

0022-3654/89/2093-5107$01.50/0 © 1989 American Chemical Society

are not stiff, one seeks the most efficient algorithm for calculating the MEP to reduce the numbers of gradient calculations required to achieve an accurate path for the particular application.[4,7,8] If more sophisticated, more specialized, or higher order techniques permit a larger step, this will usually more than balance the greater amount of computational overhead required for the more complex methods; this in turn reduces the computer time required for a given level of electronic structure theory. An example of a more sophisticated approach[7] has recently been applied to the isomerization of Si_2H_2.[7d]

Section 3 of this paper will illustrate the use of both stiffly stable techniques and high-order methods for the reaction

$$CH_3 + H_2 \rightarrow CH_4 + H \qquad (R1)$$

and it will compare them to the lowest order, non-stiffly-stable Euler method, with and without reaction path stabilization.

On the basis of these comparisons, we can assess the numerical reliability of the computed MEP for the chosen level of electronic structure theory, and in section 4, we illustrate the use of a reaction path and harmonic potential around it for a complete calculation of a bimolecular rate coefficient, including tunneling. This is accomplished by interfacing a standard electronic structure code, GAUSSIAN82,[9] to the POLYRATE code[10] for variational transition-state theory[11] and semiclassical tunneling[11] calculations. Dynamics calculations based directly on electronic structure energy and energy derivatives without the intermediary of a potential energy surface fit are called direct dynamics. The direct dynamical calculation of unimolecular rate coefficients was reported earlier by Gray et al., Tachibana et al., and Colwell et al.,[12] and the present article demonstrates the feasibility of direct dynamics calculations for bimolecular rate coefficients. Our calculations include all degrees of freedom of the six-atom system and include reaction path curvature effects in the tunneling calculations.

2. Methods

Once the conventional transition-state structure, i.e., saddle point, has been determined, a minimum energy path can be followed down to the reactants on one hand and to the products on the other, by one of several possible schemes. A convenient definition of the reaction path is the path of steepest descents in mass-weighted or mass-scaled coordinates;[13-15] this has been called the intrinsic reaction coordinate (IRC),[14] and it is especially well suited to dynamics calculations based on reaction path potentials.[3,13,16,17] The differential equations defining the IRC have the following form in mass-weighted Cartesian coordinates x_μ:

$$(m_\alpha/\mu)^{1/2}X_\alpha = x_{3\alpha-2}$$

$$(m_\alpha/\mu)^{1/2}Y_\alpha = x_{3\alpha-1}$$

$$(m_\alpha/\mu)^{1/2}Z_\alpha = x_{3\alpha} \qquad \alpha = 1, 2, ..., N$$

$$dx_1/(\partial V/\partial x_1) = dx_2/(\partial V/\partial x_2) = ... = dx_{3N}/(\partial V/\partial x_{3N}) \quad (1)$$

Here, X_α, Y_α, and Z_α are Cartesian coordinates of atom α, m_α is the mass of atom α, μ is an arbitrary reduced mass, and V represents the potential energy. We will take reaction path, IRC, and MEP to be synonymous in this paper.

The optimum choice of methodology to solve the IRC equations (1) is dependent on both the accuracy required and the particular system under study. For example, for semiclassical dynamics calculations it is necessary to obtain an especially well-converged path.[3,4,16,17] We will consider several possible algorithms, which are summarized below. The following notation will be used: the coordinate s measures distance along the MEP, and s_n is the distance along the reaction path at point $\mathbf{x}_n$, where $\mathbf{x}_n$ denotes a vector with components $x_\mu(s_n)$. The origin of s is at the saddle point geometry. The unit vector in the opposite direction from the gradient of the potential at point $\mathbf{x}$ is called $\mathbf{v}(\mathbf{x})$. The numerical derivative of $\mathbf{v}$ is

$$\mathbf{v}_{ij}' = [\mathbf{v}(\mathbf{x}_i) - \mathbf{v}(\mathbf{x}_j)]/(s_i - s_j)$$

The quantity $s_n - s_{n-1}$ is variously called the step size, δs, or the stride.

Since the gradient at the saddle point is zero, the MEP is initiated by making a small displacement in the direction of the imaginary normal mode. Within the harmonic approximation, the energy lowering, ΔE, for a given step, h, is approximately

$$\Delta E = \tfrac{1}{2}k_{ss}h^2$$

where k_{ss} is the negative force constant, and the step size h is chosen to produce a desired energy lowering, which was taken as $10^{-4}E_h$ (where $E_h \equiv 1$ hartree).

GAUSSIAN82,[9] modified locally to integrate eq 1 by various methods and to output geometries, energies, gradients, and Hessians at selected points along the MEP, was used to generate reaction paths for the abstraction reaction (R1).

Sections 2.1 and 2.2 list the methods to be considered here and present convenient abbreviations to refer to them. Section 2.3 discusses the methods.

2.1. One-Step Methods. A. Original Euler Single-Step Method (ES).

$$\mathbf{x}_{n+1} = \mathbf{x}_n + \delta s\mathbf{v}(\mathbf{x}_n) \qquad (2)$$

This method is equivalent to the fixed-stride Adams predictor of order 0,[4] but it is sometimes called "first order" in text books. The differences in terminology arise from the fact that "order" may be assigned in various ways, e.g., either as the number of points previous to the current one at which grid information is required or as the order of the error. The Euler method is of order zero in the former scheme, but the error in the solution is first order in δs.

(6) (a) Hull, T. E. In *Information Processing 68: Proceedings of the International Federation for Information Processing Congress 1968*; Morrell, A. J. H., Ed.; North-Holland: Amsterdam, 1969; p 40. (b) Dahlquist, G. *Ibid.*; p 183. (c) Gear, C. W. *Ibid.*; p 187. (d) Krogh, F. T. *Ibid.*; p 194. (e) Osborne, M. R. *Ibid.*; p 200.

(7) (a) Page, M.; McIver, J. W., Jr. *J. Chem. Phys.* **1988**, *88*, 15. (b) Profeta, S., Jr.; Unwalla, R. J.; Cartledge, F. K. *J. Org. Chem.* **1986**, *51*, 1884. (c) Sprague, J. T.; Tai, J. C.; Yuh, Y.; Allinger, N. L. *J. Comput. Chem.* **1987**, *8*, 581. (d) Koseki, S.; Gordon, M. S. *J. Phys. Chem.*, in press.

(8) (a) Ishida, K.; Morokuma, K.; Kormornicki, A. *J. Chem. Phys.* **1977**, *66*, 2153. (b) Schmidt, M. W.; Gordon, M. S.; Dupuis, M. *J. Am. Chem. Soc.* **1985**, *107*, 2585.

(9) Binkley, J. S.; Frisch, M.; Ragavachari, K.; DeFrees, D. J.; Schlegel, H. B.; Whiteside, R.; Fluder, E.; Seeger, R.; Pople, J. A. GAUSSIAN82 program, Carnegie-Mellon University, 1983, unpublished.

(10) Isaacson, A. D.; Truhlar, D. G.; Rai, S. N.; Steckler, R.; Hancock, G. C.; Garrett, B. C.; Redmon, M. J. *Comput. Phys. Commun.* **1987**, *47*, 91.

(11) (a) Truhlar, D. G.; Isaacson, A. D.; Skodje, R. T.; Garrett, B. C. *J. Phys. Chem.* **1982**, *86*, 2252. (b) Truhlar, D. G.; Garrett, B. C. *Annu. Rev. Phys. Chem.* **1984**, *35*, 159. (c) Truhlar, D. G.; Isaacson, A. D.; Garrett, B. C. In Theory of Chemical Reaction Dynamics; Baer, M., Ed.; CRC Press: Boca Raton, FL, 1985; p 65. (d) Truhlar, D. G.; Garrett, B. C. *J. Chim. Phys. Phys.-Chim. Biol.* **1987**, *84*, 365.

(12) Gray, S. K.; Miller, W. H.; Yamaguchi, Y.; Schaefer, H. F., III *J. Chem. Phys.* **1980**, *73*, 2733. Gray, S. K.; Miller, W. H.; Yamaguchi, Y.; Schaefer, H. F., III *J. Am. Chem. Soc.* **1981**, *103*, 1900. Tachibana, A.; Okazaki, I.; Koizumi, M.; Hori, K.; Yomabe, T. *J. Am. Chem. Soc.* **1985**, *107*, 1190. Colwell, S. M.; Handy, N. C. *J. Chem. Phys.* **1985**, *82*, 128. Colwell, S. M. *Theor. Chim. Acta* **1988**, *74*, 123.

(13) (a) Shavitt, I. University of Wisconsin Theoretical Chemistry Laboratory Technical Report WIS-AEC-23, Madison, WI, 1959, unpublished. (b) Marcus, R. A. *J. Chem. Phys.* **1966**, *45*, 4493. (c) Marcus, R. A. *J. Chem. Phys.* **1968**, *49*, 2610. (d) Truhlar, D. G.; Kupermann, A. *J. Am. Chem. Soc.* **1971**, *93*, 1840.

(14) (a) Fukui, K. In *The World of Quantum Chemistry*; Daudel, R., Pullman, B., Eds.; Reidel: Dordrecht, The Netherlands, 1974; p 113. (b) Fukui, K.; Kato, S.; Fujimoto, H. *J. Am. Chem. Soc.* **1975**, *97*, 1. (c) Fukui, K. *Acc. Chem. Res.* **1981**, *14*, 36.

(15) Schaefer, H. F., III *Chem. Br.* **1975**, *11*, 227.

(16) (a) Hofacker, L. *Z. Naturforsch., A* **1963**, *18*, 6007. (b) Marcus, R. A. *Discuss. Faraday Soc.* **1967**, *44*, 7. (c) Truhlar, D. G. *J. Chem. Phys.* **1970**, *53*, 2041. (d) Garrett, B. C.; Truhlar, D. G. *J. Phys. Chem.* **1979**, *83*, 1052; **1983**, *87*, 4553(E). (e) Miller, W. H.; Handy, N. C.; Adams, J. E. *J. Chem. Phys.* **1980**, *72*, 99. (f) Isaacson, A. D.; Truhlar, D. G. *J. Chem. Phys.* **1982**, *76*, 1380. (g) Miller, W. H. In *The Theory of Chemical Reaction Dynamics*; Clary, D. C., Ed.; Reidel: Dordrecht, The Netherlands, 1986; p 27.

(17) Skodje, R. T.; Truhlar, D. G.; Garrett, B. C. *J. Chem. Phys.* **1982**, *77*, 5955.

B. Euler Method with Reaction Path Stabilization,[4,8b] *Versions 2 and 3 (ES2 and ES3).* Equation 2 is corrected (stabilized) by a quadratic fit along a "bisector" line.[4,8b] The spacing, δ_2, between the points along this bisector is fixed at $0.025a_0$. In version 2, the stabilization step is applied after every Euler step, whereas in version 3 stabilization is omitted if the angle between successive gradients is less than a stabilization threshold θ_0.

C. Backward Euler Method (BE).

$$\mathbf{x}_{n+1}^{(0)} = \mathbf{x}_n + \delta s \mathbf{v}(\mathbf{x}_n) \tag{3a}$$

$$\mathbf{x}_{n+1}^{(i)} = \mathbf{x}_n + \delta s \mathbf{v}(\mathbf{x}_{n+1}^{(i-1)}) \qquad i = 1, 2 \tag{3b}$$

This method was applied with two iterates of the implicit (3b) and was stabilized as follows. If the energy at $\mathbf{x}_{n+1}^{(2)}$ was higher than that at $\mathbf{x}_n$, a new δs was defined as $0.75\delta s$, and (3a) and (3b) were repeated. When the energy condition was satisfied, the step was accepted. However, δs was reinitialized to the originally input nominal value to begin the next step.

D. Trapezoidal Euler Method (TE). Here, we again used (3a) but followed it with

$$\mathbf{x}_{n+1}^{(i)} = \mathbf{x}_n + \tfrac{1}{2}\delta s[\mathbf{v}(\mathbf{x}_{n+1}^{(i-1)}) + \mathbf{v}(\mathbf{x}_n)] \qquad i = 1, 2, \ldots \tag{4}$$

Here, we allowed for more than two iterates if necessary for convergence. In particular, beginning with the $i = 2$ iterate, we checked whether $|\mathbf{x}_{n+1}^{(i)} - \mathbf{x}_{n+1}^{(i+1)}| < \epsilon$ and repeated (4) until this was satisfied. We set $\epsilon = (6 \times 10^{-5})a_0$.

E. Runge–Kutta Method of Order 2[5b,c,m] *(RK2).*

$$k_1 = \delta s \mathbf{v}(\mathbf{x}_n)$$

$$\mathbf{x}_{n+1} = \mathbf{x}_n + \delta s \mathbf{v}(\mathbf{x}_n + \tfrac{1}{2}k_1) \tag{5}$$

F. Runge–Kutta Method of Order 4[5b,c,m] *(RK4).*

$$k_1 = \delta s \mathbf{v}(\mathbf{x}_n)$$

$$k_2 = \delta s \mathbf{v}(\mathbf{x}_n + \tfrac{1}{2}k_1)$$

$$k_3 = \delta s \mathbf{v}(\mathbf{x}_n + \tfrac{1}{2}k_2)$$

$$k_4 = \delta s \mathbf{v}(\mathbf{x}_n + k_3)$$

$$\mathbf{x}_{n+1} = x_n + (k_1 + 2k_2 + 2k_3 + k_4)/6 \tag{6}$$

In applying the RK2 and RK4 algorithms we used a fixed value of the stride δs. However, because the Runge–Kutta methods involve one to three intermediate points, $|\mathbf{x}_{n+1} - \mathbf{x}_n|$ is not a constant.

2.2. Multistep Methods. A. Quadratic Fixed-Step Adams Predictor[4,5f] *(QFAP).*

$$\mathbf{x}_{n+1} = \mathbf{x}_n + (s_{n+1} - s_n)\mathbf{v}(\mathbf{x}_n) + \tfrac{1}{2}(s_{n+1} - s_n)^2 \mathbf{v}_{n,n-1}' \tag{7}$$

This method was previously[4] called fixed-step Adams predictor of order 1 (FAP1), although, for reasons discussed in section 2.1.A, it may also be called second order; to avoid confusion we now call it QFAP.

B. Fixed-Stride Adams–Bashforth Method of Order 2[5h] *(FAB2).*

$$\mathbf{x}_{n+1} = \mathbf{x}_n + \tfrac{1}{2}\delta s[3\mathbf{v}(\mathbf{x}_n) - \mathbf{v}(\mathbf{x}_{n-1})] \tag{8}$$

C. Adapted-Stride Adams–Moulton Predictor–Corrector Method of Order 3 (AM3).

$$\mathbf{x}_{n+1}^{(0)} = \mathbf{x}_n + (\delta s^{(0)}/12)[23\mathbf{v}(\mathbf{x}_n) - 16\mathbf{v}(\mathbf{x}_{n-1}) + 5\mathbf{v}(\mathbf{x}_{n-2})] \qquad i = 0, 1 \tag{9a}$$

$$\delta s^{(1)} = \delta s^{(0)}(14\epsilon/3|\mathbf{x}_{n+1}^{(1)} - \mathbf{x}_{n+1}^{(0)}|)^{1/(p+1)} \tag{9b}$$

$$\mathbf{x}_{n+1}^{(i)} = \mathbf{x}_{n+1}^{(0)} + (\delta s^{(i-1)}/12)[5\mathbf{v}(\mathbf{x}_{n+1}^{(0)}) + 8\mathbf{v}(\mathbf{x}_n) - \mathbf{v}(\mathbf{x}_{n-1})] \qquad i = 1, 2 \tag{9c}$$

Notice that (9b) is similar to standard algorithms[5g,j] for variable-stride methods, but in our implementation, $\delta s^{(0)}$ was set equal to the originally input nominal δs at the start of each new step. Again, we set $\epsilon = 5 \times 10^{-6}a_0$. The final result of the step is $\mathbf{x}_{n+1}^{(2)}$.

D. Adapted-Stride Adams–Moulton Predictor–Corrector Method of Order 4 (AM4).

$$\mathbf{x}_{n+1}^{(i)} = \mathbf{x}_n + (\delta s^{(i)}/24)\{55\mathbf{v}(\mathbf{x}_n) - 59\mathbf{v}(\mathbf{x}_{n-1}) + 37\mathbf{v}(\mathbf{x}_{n-2}) - 9\mathbf{v}(\mathbf{x}_{n-3})\} \tag{10a}$$

$$\mathbf{x}_{n+1} = \mathbf{x}_{n+1}^{(0)} + (\delta s^{(i)}/24)\{9\mathbf{v}(\mathbf{x}_{n+1}) + 19\mathbf{v}(\mathbf{x}_n) - 5\mathbf{v}(\mathbf{x}_{n-1}) + \mathbf{v}(\mathbf{x}_{n-2})\} \tag{10b}$$

The strides $\delta s^{(0)}$ and $\delta s^{(1)}$ for the AM4 calculations were the same as given above for AM3.

2.3. Discussion of Methods. The previous paper[4] presented an investigation of three of the methods considered here, namely the Euler and ES2 methods and the QFAP method, as well as other methods. Results from that work will be compared with the present findings which include additional one-step (BE, TE, RK2, and RK4)[3] and multistep (FAB2, AM3, and AM4) methods.

In the one-step methods, the approximation for the new MEP point, $\mathbf{x}_{n+1}$, involves information from only one of the previous solution points, $\mathbf{x}_n$. The Runge–Kutta methods also use function evaluation information at intermediate points between $\mathbf{x}_n$ and $\mathbf{x}_{n+1}$, but they do not retain that information for use in approximating new points along the MEP. All the information used by these methods is obtained within the interval over which the solution is approximated.

The Euler method is the simplest method used to solve initial value problems. The basic Euler method uses only the gradient at the previous point. The ES2 method is explained elsewhere;[4,8b] it involves reaction path stabilization steps added to the basic Euler algorithm. Since the Euler method is the most commonly used method for solving the MEP equations, it and its ES2 extension will be used to obtain "standard" results with which to test the convergence properties of other methods.

The Runge–Kutta methods were originally developed to avoid the computation of higher order derivatives required by methods based on Taylor series; extra function values are used instead of higher order derivatives. The major computational effort in applying the Runge–Kutta methods to MEP calculations is the evaluation of the additional gradients at the intermediate points. In the second- and fourth-order methods, the truncation error is $O(h^2)$ and $O(h^4)$, respectively, where $h \equiv \delta s$, while the cost is two or four function evaluations per step. Butcher[5b] noted that Runge–Kutta methods of order greater than 4 have poor stability for systems of equations.

Multistep methods require the use of the approximate solution at more than one previous point along the MEP to determine the approximation at the new point. The QFAP and Adams–Bashforth techniques are *explicit* methods; that is, they determine the next point explicitly in terms of previously determined values. The Adams–Moulton techniques are *implicit* methods, since the new point is determined by using the value of that new point. The Adams–Bashforth and Adams–Moulton techniques are typically used together and collectively called *predictor–corrector methods.* These involve the use of the Bashforth formula to make a first prediction of the next point, followed by the application of the Moulton formula[5] to make successive improvements. Predictor–corrector methods have the advantage that from successive approximations to each $\mathbf{x}_k$ value, an estimate of the error can be made. The usual procedure is to use an implicit Adams–Moulton method of order $(n - 1)$ to improve an approximation obtained from an explicit Adams–Bashforth method or order n. This combination is called a predictor–corrector method of order n.

The set of MEP equations (1) can become stiff[5,6] for some systems. Difficulties result when standard numerical techniques are applied to such problems. The only methods considered here that are suitable for stiff systems are the trapezoidal and backward Euler methods. The trapezoidal method can have unsatisfactory features[6e] for some systems, in which case the simpler backward

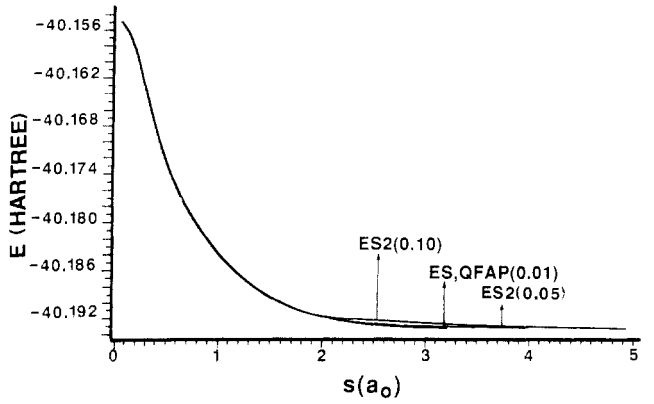

Figure 1. Energy along the reaction path obtained by Euler and QFAP algorithms with step size $0.01a_0$ and ES2 algorithm with step sizes $0.10a_0$ and $0.05a_0$ for the half reaction $CH_5^* \rightarrow CH_4 + H$. Three of the curves agree quite well over the whole range calculated, but the ES2 curve with step size $0.10a_0$ is somewhat higher in the region $(2\text{–}3^1/_2)a_0$.

Euler method is preferred. The backward Euler should allow a larger step size than non-stiffly-stable methodologies such as the original Euler method, when applied to a stiff system of equations.

3. Illustration of Methods

The methods discussed above will be illustrated with the abstraction reaction (R1). The results from the various methods will be compared with each other.

The minimum energy paths were computed by using analytic gradients computed from UHF/STO-3G[18] wave functions. A tight condition (root mean square of the gradient components less than $10^{-5}E_h a_0^{-1}$, where $a_0 \equiv 1$ Bohr radius) on the gradient was used in the location of the saddle point. The saddle point has C_{3v} symmetry and has the following geometry at the UHF/STO-3G level of calculation: R(H–H) = 0.915 Å, R(H–C) for bond formation is 1.302 Å, methyl R(C–H) = 1.083 Å, and H–C–H angle = 106.5°. The Hessian matrix at the saddle point was computed analytically.[9] The normal mode corresponding to the imaginary frequency consists primarily of transfer of an H atom from H_2 along the CH_3 rotation axis to form H and methane. The arbitrary reduced mass μ was set equal to $1u$ ($u \equiv 1$ ^{12}C atomic mass unit). Thus, distances through the mass-scaled coordinates in a_0 are equivalent to distances through mass-weighted coordinates in $u^{1/2}a_0$.

The calculated classical endoergicity and classical barrier height at this level of theory for the reaction as written in (R1) are 0.7 and 24.5 kcal/mol, respectively. The experimental classical endoergicity and classical barrier height for this reaction are estimated by Kurylo et al.[19] as −2.6 and 11.8 kcal/mol, respectively, and by two of the present authors and co-workers as −2.6[20a] and 10.1[20b] kcal/mol, respectively. Because of the large discrepancy in the calculated and experimental barrier heights, we cannot calculate accurate rate constants at this level; however, our goal is to use these calculations to compare various possible ways to calculate reaction paths and to demonstrate the feasibility of a full calculation with the direct use of ab initio input. The results illustrate the interface of the general electronic structure code GUASSIAN82[9] and the general polyatomic rate constant code POLYRATE.[10] In addition, we will demonstrate how one can use the information generated from POLYRATE, such as the adiabatic potential, projected vibrational frequencies along the path, vibrational coupling constants, curvature, transmission probabilities,

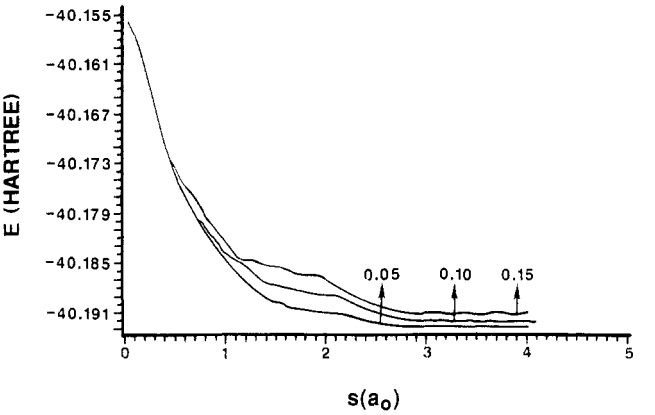

Figure 2. Energy along the reaction path obtained by TE algorithm with step sizes $0.05a_0$, $0.10a_0$, and $0.15a_0$ for the half reaction $CH_5^* \rightarrow CH_4 + H$.

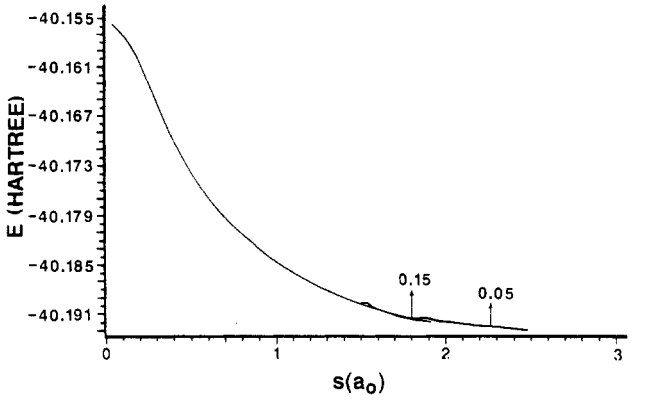

Figure 3. Energy along the reaction path obtained by BE algorithm with step sizes $0.05a_0$ and $0.15a_0$ for the half reaction $CH_5^* \rightarrow CH_4 + H$.

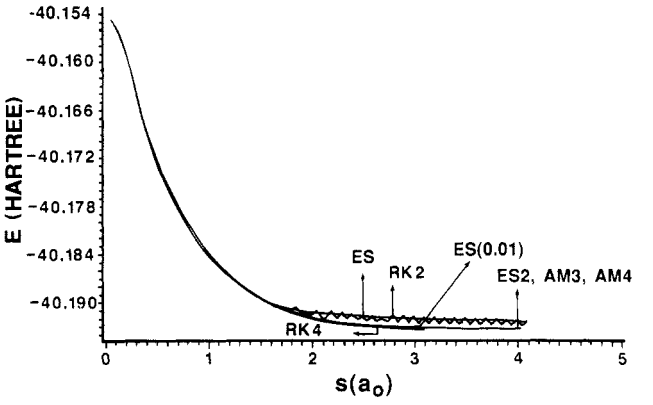

Figure 4. Energy along the reaction path obtained by Euler, ES2, RK2, RK4, AM3, and AM4 algorithms with step size $0.05a_0$ and Euler algorithm with step size $0.01a_0$ for the half reaction $CH_5^* \rightarrow CH_4 + H$.

and rate constants, to draw conclusions concerning the dynamics of the reaction.

Table Ia–c gives timing information for various calculations. Each entry refers to the computer time and number of gradient evaluations required to compute the MEP over an interval of $3.02a_0$ on one or the other side of the saddle point. The runs in Table Ia were performed on an IBM 3081 and required 0.04–0.4 h/run, whereas those in parts b and c of Table I were performed on VAX 8530 and Micro VAX II computers and require 3.5–91 h/run. For comparison purposes, relative timings between the machines were obtained and all run times were converted to a common scale on which the time for an ES2 calculation with $\delta s = 0.05a_0$ was arbitrarily set equal to unity.

Throughout this paper, negative s refers to the reactant ($CH_3 + H_2$) side of the saddle point and positive s to the product ($CH_4 + H$) side. Figures 1–7 show results for the product side of the

(18) Hehre, W. J.; Radom, L.; Schleyer, P. V. R.; Pople, J. A. *Ab Initio Molecular Orbital Theory*; Wiley: New York, 1986.
(19) (a) Kurylo, M. J.; Timmons, R. B. *J. Chem. Phys.* **1969**, *50*, 5076. (b) Kurylo, M. J.; Hollinden, G. A.; Timmons, R. B. *J. Chem. Phys.* **1970**, *52*, 1773.
(20) (a) Steckler, R.; Dykema, K. J.; Brown, F. B.; Hancock, G. C.; Truhlar, D. G.; Valencich, T. *J. Chem. Phys.* **1987**, *87*, 7024. (b) Joseph, T.; Steckler, R.; Truhlar, D. G. *J. Chem. Phys.* **1987**, *87*, 7036.

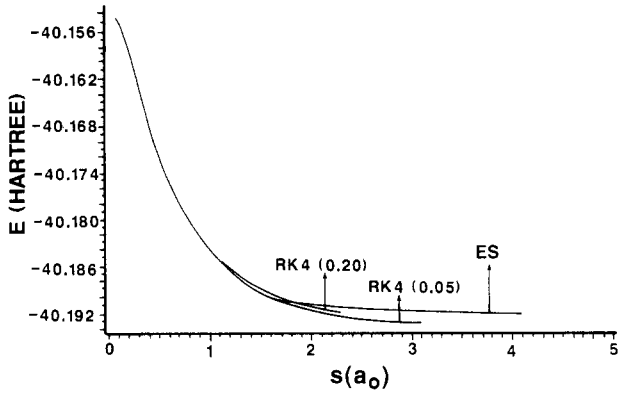

Figure 5. Energy along the reaction path obtained by Euler algorithm with step size $0.05a_0$ and RK4 algorithm with step sizes $0.05a_0$ and $0.20a_0$ for the half reaction $CH_5^\ddagger \rightarrow CH_4 + H$.

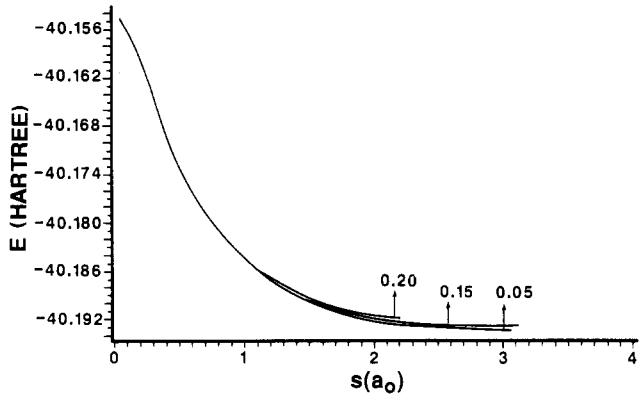

Figure 6. Energy along the reaction path obtained by RK4 algorithm with step sizes $0.05a_0$, $0.15a_0$, and $0.20a_0$ for the half reaction $CH_5^\ddagger \rightarrow CH_4 + H$.

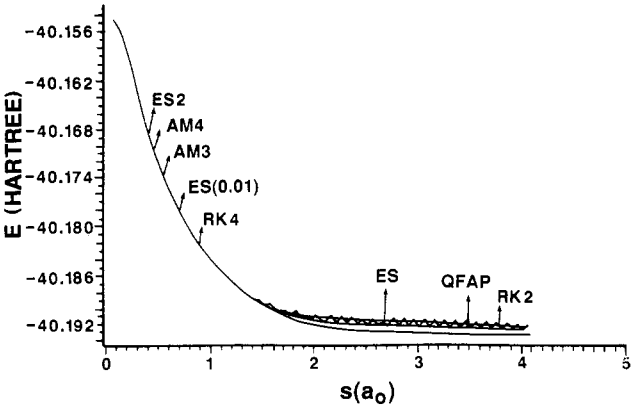

Figure 7. Energy along the reaction path from Euler, QFAP, ES2, RK2, RK4, AM3, and AM4 algorithms with step size $0.05a_0$ and Euler algorithm with step size $0.01a_0$ for the half reaction $CH_5^\ddagger \rightarrow CH_4 + H$. Five of the curves agree well over the whole range they were calculated [$(3-4)a_0$, depending on the method] and are labeled at small s; of the other three curves, QFAP is high and smooth, ES is even higher and smooth, and RK2 oscillates about ES.

MEP, and Figures 8–12 show results for the reactant side.

3.1. Single-Step and Quadratic Methods for the MEP. In this section, four single-step numerical techniques, TE, BE, RK2, and RK4, and the quadratic method will be compared for reaction R1 to the Euler and ES2 methods. The latter methods are applied with strides of $0.01–0.10a_0$, as is the quadratic method. The trapezoidal method is applied with fixed strides in the range $0.05–0.15a_0$, and the other methods are applied with one or more nominal strides in the range $0.05–0.20a_0$.

The results for $CH_5^\ddagger \rightarrow CH_4 + H$ are in Figures 1–6; those for $CH_5^\ddagger \rightarrow CH_3 + H_2$ are in Figure 8, and timings are given in Tables Ia and Ib. In all cases, the results and timings are labeled

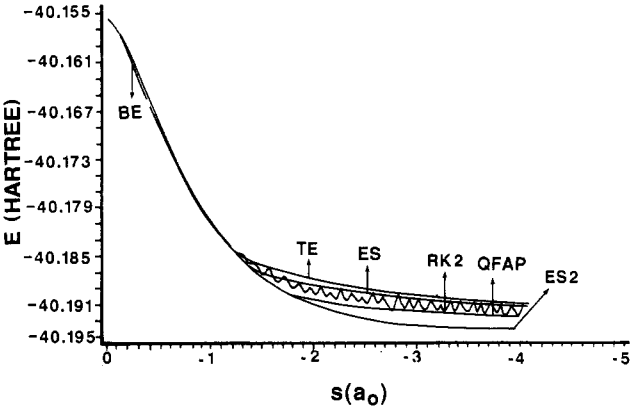

Figure 8. Energy along the reaction path obtained by Euler, ES2, QFAP, TE, BE, and RK2 algorithms with step size $0.05a_0$ for the half reaction TS $\rightarrow CH_3 + H_2$. The curve obtained by the RK2 algorithm shows spurious oscillations, and the BEM results are essentially identical to the ES2 ones over most of the range.

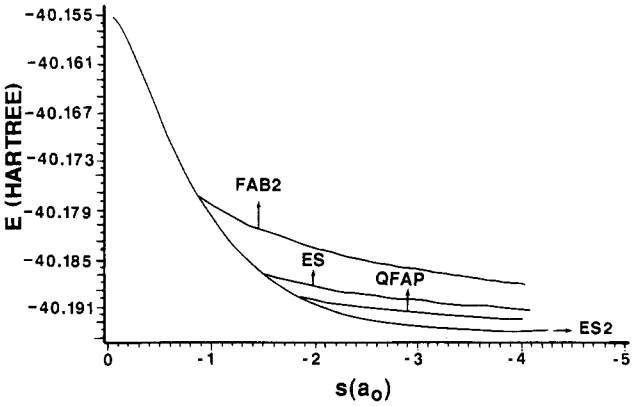

Figure 9. Energy along the reaction path obtained by Euler, ES2, QFAP, and FAB2 algorithms with step size $0.05a_0$ for the half reaction $CH_5^\ddagger \rightarrow CH_3 + H_2$.

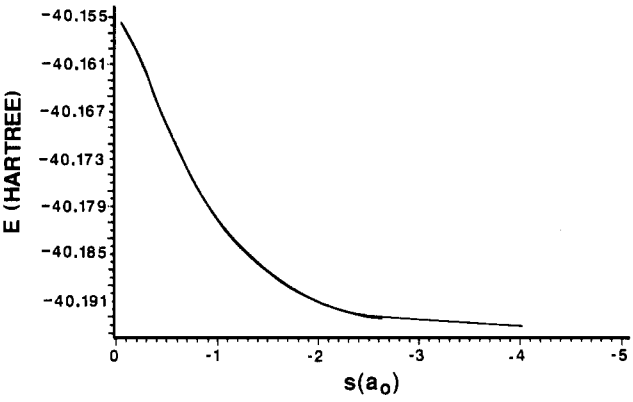

Figure 10. Energy along the reaction path obtained by AM3 algorithm with step sizes $0.05a_0$ (curve ends at $2.6a_0$) and $0.15a_0$ (curve ends at $4a_0$) for the half reaction $CH_5^\ddagger \rightarrow CH_3 + H_2$.

by the nominal (i.e., input) strides δs.

Figure 1 shows the energy along the reaction path for the product side. This figure shows that the ES2 method with stride $0.05a_0$ and the Euler (ES) and QFAP methods with stride $0.01a_0$ all provide essentially the same energy profile. Additional calculations with the ES2 method and $\delta s = 0.01a_0$ (not shown) also agree with these curves, and we therefore take this to be the converged value. Similar tests on the reactant side (not shown) yield excellent agreement between the QFAP method with $\delta s = 0.01a_0$ and the ES2 method with $\delta s = 0.05a_0$. In this direction though the ES2 method with $\delta s = 0.01a_0$ is not stable; the Euler method with $\delta s = 0.01a_0$ yields a curve just slightly higher than the converged ones.

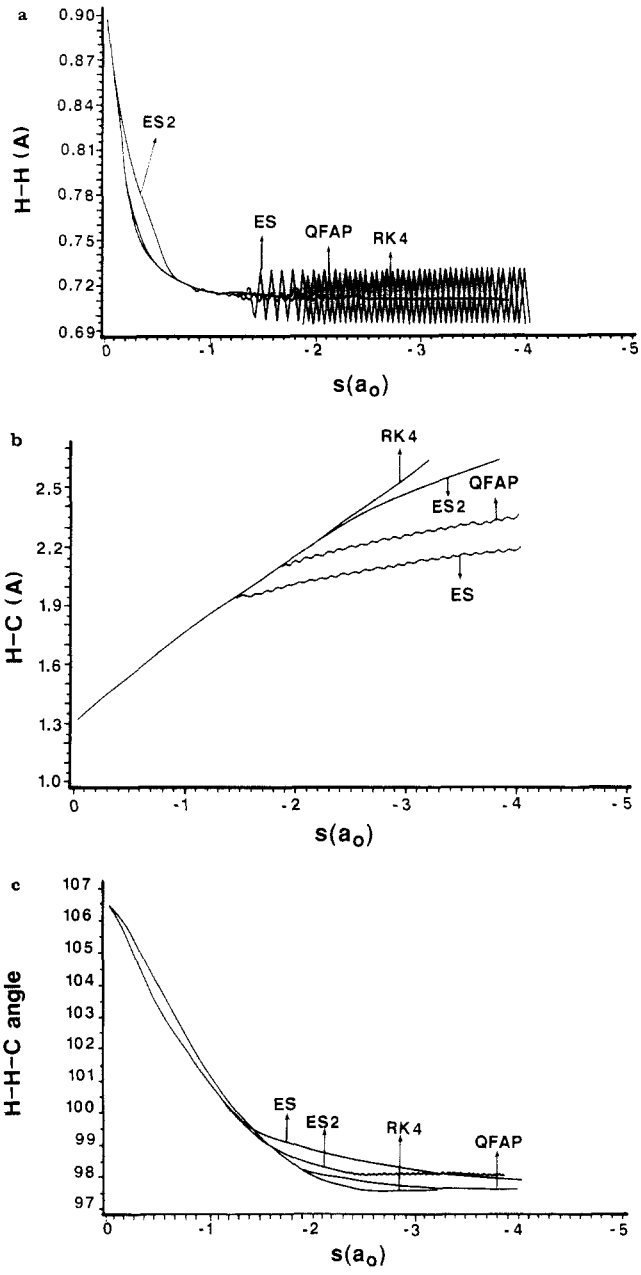

Figure 11. (a) H–H distance versus path distance from Euler, ES2, QFAP, and RK4 algorithms with step size $0.05a_0$ for the half reaction $CH_5^\ddagger \rightarrow CH_3 + H_2$. The ES and QFAP results show strong oscillations, and the RK4 curve, which ends at $3.2a_0$, shows instabilities at $1.2a_0$ and $2a_0$. (b) H–C distance versus path distance from Euler, ES2, QFAP, and RK4 algorithms with step size $0.05a_0$ for the half reaction $CH_5^\ddagger \rightarrow CH_3 + H_2$. (c) H–H–C angle versus path distance from Euler, ES2, QFAP, and RK4 algorithms with step size $0.05a_0$ for the half reaction $CH_5^\ddagger \rightarrow CH_3 + H_2$.

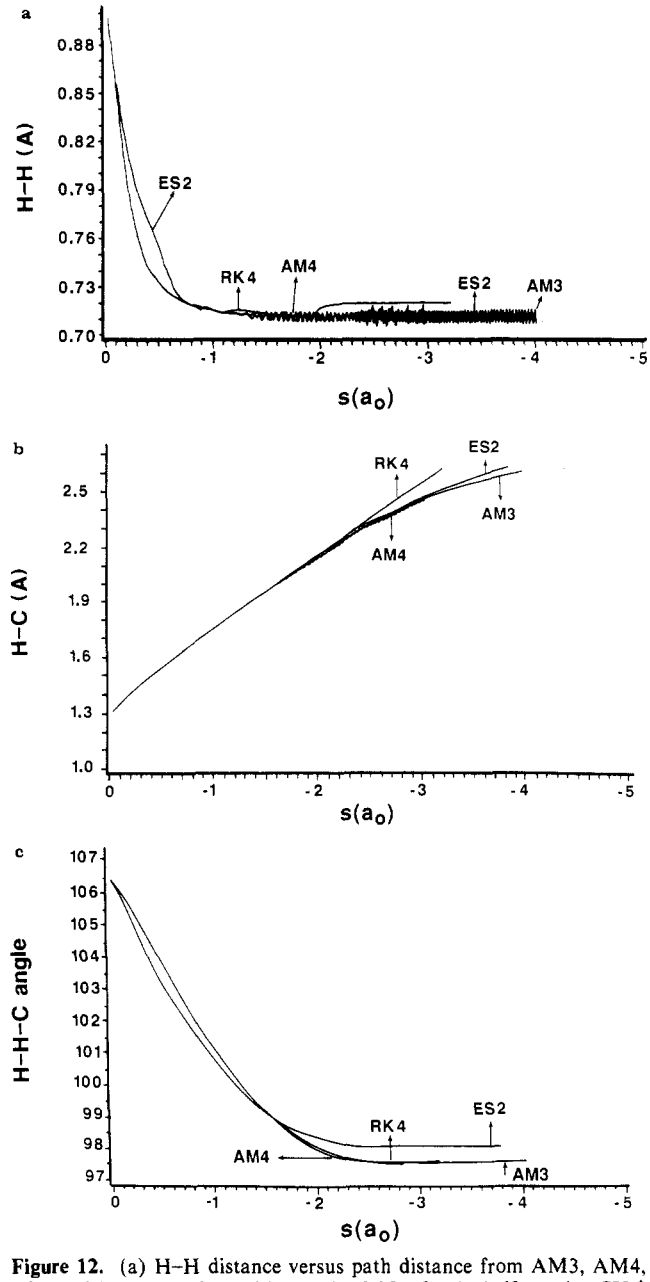

Figure 12. (a) H–H distance versus path distance from AM3, AM4, ES2, and RK4 algorithms with step size $0.05a_0$ for the half reaction $CH_5^\ddagger \rightarrow CH_3 + H_2$. The AM4 curve, which ends at $3a_0$, begins to oscillate at $s \cong 1.2a_0$ and more severely at $2.4a_0$. The oscillations in the AM3 curve grow in gradually. The ES2 curve also shows oscillations in the $(1-3)a_0$ region, but it becomes smooth in the $(3-4)a_0$ region. (b) H–C distance versus path distance for from AM3, AM4, and RK4 algorithms with step size $0.05a_0$ for the half reaction $CH_5^\ddagger \rightarrow CH_3 + H_2$. (c) H–H–C distance versus path distance from AM3, AM4, ES2, and RK4 algorithms with step size $0.05a_0$ for the half reaction $CH_5^\ddagger \rightarrow CH_3 + H_2$.

Increasing the stride to $0.10a_0$ causes large errors for both the Euler and QFAP methods (about 0.003 and 0.002 E_h, respectively, at $s = 3a_0$ and 0.009 and 0.005 E_h, respectively, at $s = -3a_0$), but an order of magnitude smaller error in the ES2 method in both directions.

The instability of the ES2 method for $\delta s = 0.01a_0$ in the reverse direction apparently occurs, as discussed previously,[4] because the computed points are very close to the MEP prior to the stabilization procedure. Then, the angle between successive gradients used in this procedure[4] becomes small, and the stabilization step becomes both unnecessary and unstable. We tried a modified algorithm, ES3, in which stabilization is omitted if the angle between successive gradients is less than a stabilization threshold θ_0. For $\delta s = 0.01a_0$, setting $\theta_0 = 2°$ did not remove the instability; however, if stabilization is performed only when the angle between successive gradients is more than 4°, the instability disappears. Since reasonably good convergence is obtained with $\delta s = 0.05a_0$ for the present application, the smaller strides are unnecessary anyway.

The TE and BE methods are very simple modifications of the original Euler approach, and because of their simplicity, they are unsatisfactory for some systems. Figure 8 demonstrates that when the same stride is used for both methods, the extra computational effort of the TE method (a factor of 1.5; see Table Ib) does not provide additional accuracy relative to the results of the ES2 method. In addition, an increase in the step size appears to increase the instability of the method, as shown in Figure 2 for the forward direction (the errors are even larger for a given δs for the reverse direction, which is not shown).

The backward Euler (BE) technique, on the other hand, does

TABLE I: CPU Time and Number of Steps for the Reaction $CH_3 + H_2 \rightarrow CH_4 + H$

a. ES, QFAP, and ES2 Methods

		Euler (ES)		quadratic (QFAP)		ES2	
integration range, a_0	δs, a_0	time[a]	N[b]	time	N	time	N
0 to −3.02	0.01	1.6	301	1.7	325	1.2	98[c]
	0.05	0.3	61	0.4	80	1.0	84
	0.10	0.2	31	0.2	44	0.6	40
0 to +3.02	0.01	1.7	301	1.8	314	4.1	304
	0.05	0.4	61	0.4	68	1.0	74
	0.10	0.2	31	0.2	36	0.7	43

b. BE, TE, and Runge–Kutta Methods

		backward Euler (BE)		trapezoidal (TE)		Runge–Kutta (RK2)		Runge–Kutta (RK4)	
integration range, a_0	δs, a_0	time[a]	N[b]	time	N	time	N	time	N
0 to −3.02	0.05	3.7	271	1.5	61	0.7	61	3.5	240
	0.10			1.7	101				
	0.15	5.4	275	1.2	67			3.8	249
	0.20							3.8	250
0 to +3.02	0.05	5.7	292	2.3	126	0.7	263	4.3	263
	0.10			1.8	92				
	0.15	4.1	296	1.4	79			4.3	267
	0.20							4.0	248

c. Adams–Moulton Methods

		AM3		AM4	
s range, a_0	δs, a_0	time[a]	N[b]	time	N
0 to −3.02	0.05	2.7	230	3.1	219
	0.10	2.1	177		
	0.15	1.7	109	1.8	54
	0.20				[d]
0 to +3.02	0.05	2.8	233	2.7	225
	0.10	2.3	184		
	0.15	1.9	155	1.4	115
	0.20			1.3	109

[a] Ratio of CPU time for the indicated method and step size to that of the ES2 method with step size $0.05a_0$. [b] N is the number of steps. [c] This number is very small because, as discussed in ref 4, the ES2 method breaks down for very small step sizes. [d] Small interatomic distances were encountered when too large a step is taken for large s for this particular half reaction.

appear to improve the convergence of the reaction path. In particular, Figure 8 shows that for a nominal stride of $0.05a_0$, the BE method gives comparable accuracy to the ES2 method for the same step size. In addition, specification of larger strides gives an essentially identical path (see, e.g., Figure 3 for the forward direction of reaction; the accuracy with $\delta s = 0.15a_0$ is even better for the reverse direction of reaction, which is not shown). One must keep in mind, however, that, unlike the Euler method, the BE method yields nonconstant values for $|\mathbf{x}_{n+1} - \mathbf{x}_n|$, and the variation turns out to be larger than for the ES2 algorithm. Thus, for some portions of the path, the step actually taken may be much smaller than the stride. The BE method was implemented with a stride condition involving the energy at successive points, and for this reason, specification of too large a step can use more time than one of smaller step, since the former can require more repeated steps. Table Ib illustrates this behavior by comparing the CPU time required to generate the BE paths with strides of $0.05a_0$ and $0.15a_0$ for the reverse reaction. Also, note that the BE method requires a significant increase in computational effort (a factor of 2.3–5.4; see Table Ib) as compared to either the Euler method with $\delta s = 0.01a_0$ or the ES2 method with $\delta s = 0.05a_0$.

The other single-step techniques considered here are the Runge–Kutta methods of orders 2 and 4. Runge–Kutta methods are often used to find starting values for the Adams-type methods, but if the function evaluations are simple, they can be very useful on their own. This is illustrated in Figure 4 where a comparison is made of the Runge–Kutta methods of order 2 and 4, and the latter is found to yield good accuracy. Figures 4 and 8 both clearly illustrate the instability of the lower order method—oscillations in the energy occur very early along the computed path and continue throughout its course. Although the method of order 4 requires twice as many function evaluations, it has a truncation error that is 2 powers of δs smaller than the method of order 2. (The significant difference in computation times for the RK2 and RK4 paths are a consequence of the instability of the lower order method.)

The path calculated by the RK4 method is also compared with the converged paths obtained by the ES2 method with stride $0.05a_0$ and with the Euler method with stride $0.01a_0$ in Figure 4. The RK4 path generated with a nominal stride of $0.05a_0$ is superimposable with both of these curves. In addition, Figure 6 shows that one can use a large stride with this method without greatly sacrificing accuracy, and Figure 5 illustrates that the RK4 method is more accurate than the Euler method for this test problem. Recall, however, that for the same stride the RK4 method requires four function evaluations for every one functional evaluation of the Euler method. Furthermore, in comparison to the BE method, the RK4 procedure yields an even wider variation in the actual length of the step taken, i.e., in $|\mathbf{x}_{n+1} - \mathbf{x}_n|$. Examination of the step sizes actually taken during an RK4 run with a nominal stride of $0.20a_0$ demonstrates that portions of the curve are generated with step sizes as small as $0.001a_0$ or even smaller. It turns out that utilization of a nominally small stride is sometimes *more* efficient than use of a larger one (see Table Ib). As a consequence, the actual CPU time required to generate the various RK4 curves are 2.2–3.8 times longer than that for the ES2 (stride $0.05a_0$) and Euler (stride $0.01a_0$) methods (see Table Ib). Although the RK4 method requires more computational effort than it takes to generate a converged Euler or ES2 path, it may be useful in some cases for increased accuracy.

Figure 11a–c illustrates the variation in internal coordinates with the distance along the reaction path on the reactant side for several single-step methods. From Figure 11a, one can see that, for all methods but the RK4 method, there are oscillations in the H–H parameter as one moves away from the saddle point and the RK4 method also shows some instability. Even at $3.1a_0$, the

TABLE II: Oscillations in the H-H Distance Along the Calculated MEP for $CH_5^+ \rightarrow CH_3 + H_2$

method	δs, a_0	s value where oscillations start, a_0	eventual width of oscillations, Å
Euler	0.01	−2.2	0.01
	0.05	−1.3	0.04
	0.10	−0.4	0.07
QFAP	0.01	−2.5	0.01
	0.05	−1.8	0.04
	0.10	−0.4	0.07

RK4 curve has not converged to the correct value for the H-H distance; this illustrates one of the pitfalls of MEP calculations, namely that even though the RK4 method might be accurate in this region if the integration were on the correct path, errors earlier in the calculation have placed it on an incorrect path that is not quickly corrected. Similar results are obtained for the variation in the H-C bond distance (Figure 11b), except that for this coordinate the ES2 method gives smooth variation as a function of s as well. Overall, the RK4 algorithm yields a slightly better converged path for this coordinate.

In general, the oscillations in internal coordinates become larger and begin earlier as δs is increased. Table II gives some examples for the Euler and QFAP methods on the reactant side.

3.2. Multistep Methods for the MEP. Figures 4, 7, 9, 10, and 12 show some of the results obtained with multistep methods and compare them to selected single-step results.

To illustrate the power of the corrector formula in the Adams–Moulton predictor–corrector methods, an MEP was generated with utilization of only the Adams–Bashforth predictor method of order 2 (FAB2). This can be compared to the quadratic method for stability. Figure 9 shows the results of such a comparison. Notice that the FAB2 curve is actually much less converged than that obtained with even the simple Euler method with the same step size. In general, the Adams–Bashforth techniques alone are relatively unstable methods. An explanation for this is provided by comparison of an m-step Adams–Bashforth explicit method with an $(m-1)$-step Adams–Moulton implicit method. Both require m evaluations of the function per step, and both have a local truncation error proportional to $(\delta s)^m$. In general, the coefficients of the terms involving the function and the local truncation error are smaller for the Adams–Moulton methods [see, e.g., eq 9a versus 9b or 10a versus 10b]. This leads to greater stability for the implicit methods and a smaller rounding error. Thus, as is well-known, the best compromise is to utilize the explicit methods for prediction of a new point, followed by refinement of this prediction with the Adams–Moulton corrector step.

Figure 4 shows the results obtained with the AM3 and AM4 methods for the forward direction of reaction R1; it is clear from this figure that, for this reaction with $\delta s = 0.05a_0$, the methods are identical in accuracy. Similar good agreement is found with this stride for the reverse direction; Figure 10 shows that the AM3 method is very stable with respect to increasing the stride. A comparison of the amount of CPU time necessary to generate the respective curves for the AM3 and AM4 methods (Table Ic) indicates that both also require similar computer time. Notice from Table Ic that the CPU time for the AM3 calculations decreases by a factor of $1^1/_2$–2 when one increases the nominal stride by a factor of 3, but that for the AM4 calculations is less predictable (the reason is probably similar to that discussed in section 3.1 with respect to the RK4 algorithm). The computational effort for the Adams–Moulton calculations is somewhat greater than that for well-converged Euler and ES2 calculations.

The Adams–Moulton methods used here involved stride adaptation. Two approximations (one from the predictor and one from the corrector) are available for each MEP point, and comparison of these allows one to estimate the uncertainty in the step. The difference in these two approximations (the error approximation) is then used to adapt the stride. (The algorithm is given in section 2.2.) This stride adaptation controls the local truncation error as well as the global error as one proceeds along the path, and it allows one to specify a larger nominal stride and still retain good accuracy in difficult-to-integrate regions.

A comparison of the multistep methods with various other methods is shown in Figure 7. These show that the Adams–Moulton methods give results comparable to those obtained with the Euler method with a very small step size as well as with the RK4 method. Figure 12 shows the variance of internal degrees of freedom for the multistep methods as compared to the RK4 method and the "standard" ES2 method. Figure 12a illustrates the variance in H–H bond distance with the distance along the reaction path. There is still significant unrealistic oscillation with the multistep methods, indicating instability. The variance in the H–H–C angle, however, is similar to what is observed with the RK4 method. The better stability of this parameter may be a consequence of the fact that it changes little along the reaction path.

3.3. Recommendations. The criteria on which a comparison of the methods can be based include the number of function evaluations or CPU time required for a given accuracy and the accuracy of the method for a given computational effort. The comparison of methods also depends in part on where one needs the reaction path information and which reaction path properties (e.g., geometries, vibrational frequencies, curvature of the reaction path) will be used. On the basis of these criteria and the different possible uses for a reaction path calculation, it is probable that no single method is always best. The best choice will probably also depend on the particular reaction system being studied. One can, however, at least assess the behavior of methods within each class and extract some useful guidelines as to which methods might be recommended for general use.

We recommend that one should first try one of the simple methods (Euler, QFAP, ES2) for applications that require only qualitative information about the reaction path (for example, verification that a particular transition state leads to an indicated set of reactants and products) and for other more quantitative applications in which the reaction path equations are known to be nonstiff. If one knows ahead of time that a particular reaction path calculation involves stiff equations, then a stiff method may be preferable. If one requires particularly high accuracy, the higher order methods might become more competitive.

Among the Euler, QFAP, and ES2 methods, it appears that the method of choice for the present system is the ES2 method. The stabilization algorithm works very well for this problem. The ES2 method also performed well in our previous tests[4] although we previously recommended the Euler method because of the difficulties sometimes encountered by the ES2 algorithm when the stride is small. Although the ES2 method is computationally more expensive than the Euler and QFAP methods for a given step size, a larger step may be used (see Figure 1). For more complex systems, however, where function evaluations are more costly, it is possible that one may be better off choosing the Euler or QFAP methods with a smaller step. Although we again found, as was also found previously,[4] that the ES2 method breaks down if the stride is too small, we found that the instability disappears if the stabilization is performed only when the angle between successive gradients is more than a preselected stabilization threshold θ_0. This selective application of the stabilization step is called ES3, and it appears to fix the most serious defect of the ES2 method.

Of the TE, BE, and Runge–Kutta methods tested, only the BE and RK4 methods appear to be competitively reliable as compared with the ES2 method (see, e.g., Figure 4). The fourth-order Runge–Kutta method performs better than the second-order one, and it appears to be the most stable of these four methods for the present test case. In addition, it allows one to efficiently use a larger stride than the BE method.

It will be most interesting to test the RK4 method for more systems, particularly for complicated reactions, even though this method takes slightly more computer time than some other methods, since the RK4 method not only competes with both the single-step ES2 method and the Adams methods in convergence properties, but it also shows very good stability. It would also be interesting to test variable-stride Runge–Kutta methods.

The Adams–Moulton predictor–corrector methods are probably the best of the nonstiff multistep formulas for general computation.[5] Results given in above text indicate that these methods are reliable in predicting a converged reaction path within a reasonable amount of computer time. However, many problems are not particularly appropriate for *any* sort of multistep method. The intervals of integration may be so short that the multistep methods have little chance to demonstrate their advantage over the Runge–Kutta methods. The plots with the results of the AM and RK4 methods (e.g., Figure 7) and timings from Table Ib,c illustrate the similarities in performance of these methods for reaction R1.

4. Dynamics

Once a sufficient portion of the potential energy surface is known, it is in principle possible to calculate the reaction rate constant, k, as a function of temperature. A particularly appealing method for such calculations is variational transition-state theory (VTST) with semiclassical adiabatic ground-state (SAG) transmission coefficients.[3,11,21] The VTST method is an improvement on conventional TST,[22] which assumes that the net rate of forward reaction at equilibrium is given by the flux of trajectories across the critical dividing surface that passes through the saddle point ($s = 0$) in the direction of products.[23] In contrast, in VTST, the location of the dividing surface through which the equilibrium flux in the product direction is calculated is varied to obtain the minimum rate constant, which may be rigorously motivated[24] in classical mechanics; this provides the foundation on which to add quantal effects. From a thermodynamic point of view, one considers entropic and zero-point effects on the location of the transition state with VTST, and the SAG coefficients introduce tunneling. Whereas a conventional TST calculation requires only the barrier height and saddle point and reactant properties, and the CVT rate constant for the present case requires treating only a small range of s near zero (i.e., near the saddle point), to be treated accurately, the rate constant derived from VTST with SAG transmission coefficients depends not only on the barrier height and saddle point and reactant properties but also on the shape of the reaction path and the s dependence of the associated transverse vibrations over a wide range of s.

For a generalized transition state (GTS) that intersects the MEP at some nonzero value of s, the generalized TST rate constant at temperature T, without tunneling, is expressed in terms of equilibrium partition functions of the reactants and a quasi-equilibrium partition function of the generalized transition state as described elsewhere.[3,11,21]

We consider six approximations to the rate constant; the first three are k^{CVT}, corresponding to canonical variational transition-state theory,[3,11,21] $k^{CVT/MEPSAG} = \kappa^{CVT/MEPSAG}k^{CVT}$, and $k^{CVT/SCSAG} = \kappa^{CVT/SCSAG}k^{CVT}$, where the transmission coefficients[17,21] are labeled CVT/XSAG since they must be consistent with the CVT version of VTST and because they are semiclassical

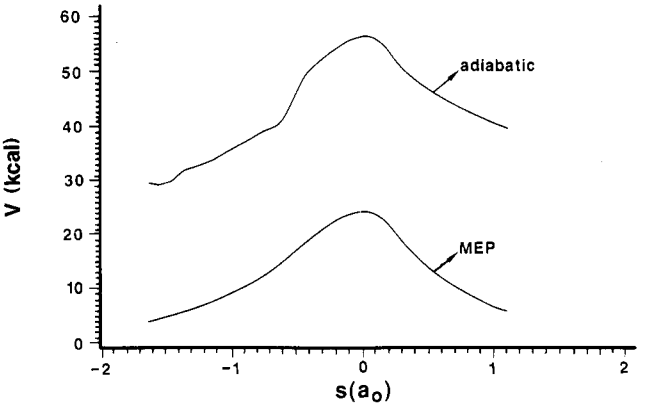

Figure 13. Classical potential energy and vibrationally adiabatic ground-state potential energy along the reaction path for the reaction $CH_3 + H_2 \rightarrow CH_4 + H$.

(S) calculations based on the adiabatic ground-state (AG) potential curve. X = MEP denotes a transmission coefficient based on tunneling along the minimum energy path (MEP), and X = SC denotes inclusion of negative internal centrifugal effects on the tunneling path in the small-curvature approximation.[17,21] We also consider the three corresponding calculations in which CVT is replaced by improved CVT (ICVT, see text below). These transmission coefficients are calculated as described in ref 4 and 11c.

The reaction path curvature is a scalar for collinear three-atom systems and a vector in general. The components of this vector along the generalized normal modes are referred to as $B_{kF}(s)$,[11c,15e,25a] where F indicates the reaction coordinate and there are $F - 1$ generalized normal modes, k. Each $B_{kF}(s)$ is a scalar product of the generalized normal mode vector of a vibration k and the derivative of the normal mode with respect to the reaction coordinate s. If the $\{B_{kF}(s)\}$ are not negligible, then motion along the reaction path is dynamically coupled to the transverse vibrations. The total curvature of the reaction path is defined as

$$\kappa(s) = \{\sum_{k=1}^{F-1} [B_{kF}(s)]^2\}^{1/2} \tag{11}$$

In the present case, we follow the spectroscopic convention of assigning a single mode number n to degenerate modes. The components are labeled m_n, and the reaction coordinate is still labeled F. Then, if d_n is the degeneracy of mode n, eq 11 becomes

$$\kappa(s) = \{\sum_{n=1}^{F-1} \sum_{m_n=1}^{d_n} [B_{nm_nF}(s)]^2\}^{1/2} \tag{12}$$

and F is now a smaller number. If $\kappa(s)$ were zero, the SCSAG transmission coefficient would reduce to the MEPSAG one. When it is not zero, the SCSAG transmission coefficient accounts for the curvature coupling of transverse coordinates to the MEP in determining the optimum tunneling path and hence it provides a multidimensional estimate of the tunneling contributions to the reaction rate.

All calculations in this paper employ the harmonic approximation for vibrations. The CVT and MEPSAG calculations require only the MEP, the potential energy along it, and the vibrational frequencies for a sequence of generalized transition states. SCSAG transmission coefficients depend on these quantities plus the $B_{kF}(s)$ curvature elements.

The MEP was generated by the ES2 method with step size $0.05a_0$, and this path was utilized in POLYRATE to study the dynamics of reaction R1. A preliminary run with the Euler MEP, again computed with $\delta s = 0.05a_0$ and with force fields performed every third point, revealed that the major contribution to tunneling occurs between $s = -1.18a_0$ and $1.10a_0$. Thus, the ES2 calculation

(21) (a) Truhlar, D. G.; Garrett, B. C. *Acc. Chem. Res.* **1980**, *13*, 440. (b) Garrett, B. C.; Truhlar, D. G. *J. Phys. Chem.* **1979**, *83*, 1079; **1983**, *87*, 4553(E). (c) Garrett, B. C.; Truhlar, D. G.; Grev, R. S.; Magnuson, A. W. *J. Phys. Chem.* **1980**, *84*, 1730; **1983**, *87*, 4554(E). (d) Skodje, R. T.; Truhlar, D. G.; Garrett, B. C. *J. Phys. Chem.* **1982**, *85*, 3019. (e) Truhlar, D. G.; Isaacson, A. D.; Skodje, R. T.; Garrett, B. C. *J. Phys. Chem.* **1982**, *86*, 2252.

(22) See for example: (a) Glasstone, S.; Laidler, K. J.; Eyring, H. *Theory of Rate Processes*; McGraw-Hill: New York, 1941. (b) Johnston, H. S. *Gas Phase Reaction Rate Theory*; Ronald Press: New York, 1966. (d) Laidler, K. J. In *Theories of Chemical Reaction Rates*; McGraw-Hill: New York, 1969; p 42. (e) Weston, R. E.; Schwartz, H. A. *Chemical Kinetics*; Prentice-Hall: New York, 1972. (f) Rapp, D. *Statistical Mechanics*; Holt, Rinehard, and Winston: New York, 1972. (g) Nikitin, E. E. *Theory of Elementary Atomic and Molecular Processes in Gases*; Clarendon Press: Oxford, U.K., 1974. (h) Smith, I. W. M. *Kinetics and Dynamics of Elementary Gas Reactions*; Butterworths: London, 1980.

(23) (a) Wigner, E. *Trans. Faraday Soc.* **1938**, *34*, 29. (b) Jaffe, R. L.; Henry, J. M.; Anderson, J. B. *J. Chem. Phys.* **1973**, *59*, 1128. (c) Pechukas, P. In *Dynamics of Molecular Collisions*; Miller, W. H., Ed.; Plenum Press: New York, 1976; Part B, p 269.

(24) (a) Keck, J. C. *J. Chem. Phys.* **1967**, *13*, 85. (b) Miller, W. H. *J. Chem. Phys.* **1974**, *61*, 1823. (c) Garrett, B. C.; Truhlar, D. G. *J. Chem. Phys.* **1979**, *70*, 1593. (d) Garrett, B. C.; Truhlar, D. G. *J. Phys. Chem.* **1979**, *83*, 1052; **1983**, *87*, 1553(E).

(25) (a) Miller, W. H. In *Potential Energy Surfaces and Dynamics Calculations*; Truhlar, D. G., Ed.; Plenum: New York, 1981; p 265. (b) Garrett, B. C.; Truhlar, D. G.; Grev, R. In *Ibid.*; p 587.

TABLE III

a. UHF/STO-3G Harmonic Frequencies and Corresponding Accurate Frequencies (cm^{-1})

frequency	UHF/STO-3G	accurate[a]
	CH_4	
$\nu_1(a_1)$	3527	2917
$\nu_2(e)$	1904	1534
$\nu_3(t_2)$	3788	3019
$\nu_4(t_2)$	1675	1306
	CH_3	
$\nu_1(a_1')$	3553	3002
$\nu_2(a_1'')$	585	580
$\nu_3(e)$	3828	3184
$\nu_4(e)$	1690	1383
	H_2	
ν	5482	4401

b. UHF/STO-3G Harmonic Frequencies for the CH_5 Transition-State Geometry

frequency	UHF/STO-3G	J3[b]	PolCI/DZP[c]
$\nu_1(a_1)$	3566	3006	3228
$\nu_2(a_1)$	1810	1628	1960
$\nu_3(a_1)$	1445	1129	995
$\nu_4(e)$	3794	3068	3404
$\nu_5(e)$	1773	1376	1534
$\nu_6(e)$	1550	1202	1146
$\nu_7(e)$	721	586	592
$\nu_8(a_1)$	2740i	1088i	974i

c. Energetic Properties for the Reaction $CH_3 + H_2 \rightarrow CH_4 + H$

property, kcal/mol	UHF/STO-3G	accurate
reactant ZPE[d]	29.5	24.5[e]
product ZPE	33.9	27.1[e]
ΔE	0.67	−2.6[f]
$\Delta H°$	−3.73	+0.02[g]
V^*	24.5	10.1[h]
ΔV_a^{*G}	27.2	11.9[h]

[a] Most accurate available: ref 28 and 29. [b] Semiempirical analytic surface; see ref 20b. [c] Ab initio calculations based on polarization configuration interaction with a double-ζ plus polarization basis set; see ref 28. [d] Zero-point energy (harmonic). [e] Computed with the harmonic approximation and the frequencies found in the JANAF tables; see ref 19, 20, and 29. [f] Classical endoergicity computing with other energies as given in this column. [g] Computed from the JANAF tables. [h] Best available estimate of harmonic zero-pointed corrected barrier height evaluated at the saddle point, from ref 20b.

of the MEP was performed in this region. Force fields were computed at every third MEP point.

Figure 13 shows a plot of the potential energy along the MEP and the vibrationally adiabatic ground-state potential curve[3,11,16,17,21,25b,26] as a function of the distance along the MEP. Notice from the comparison of these two curves that the vibrationally adiabatic barrier is slightly thinner than the bare barrier. The quantum effect of adding zero-point vibrational energy to the classical potential curve has the effect of making it easier for tunneling to occur for a given energy deficit below the top of the barrier. This is opposite to the direction of the effect in the well-studied collinear $H + H_2$ reaction without bends.[27]

Some properties of the potential in the valley along the MEP are shown in parts a–c of Table III. Table IIIa gives harmonic frequencies for H_2, CH_3, and CH_4 along with the most accurate available values,[28,29] and Table IIIb gives the harmonic frequencies for the saddle point. Table IIIc gives harmonic zero-point information calculated from these frequencies, the overall ΔE and

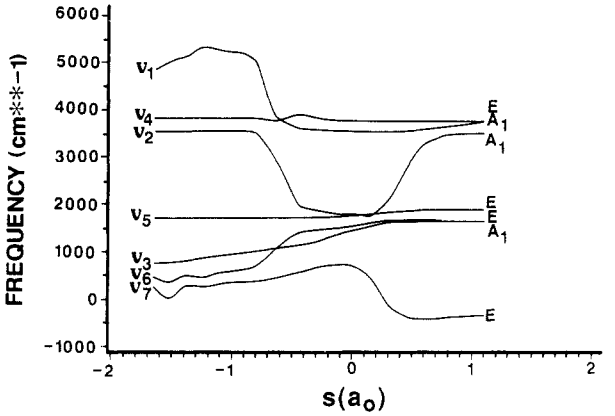

Figure 14. Projected harmonic frequencies along the reaction path for the reaction $CH_3 + H_2 \rightarrow CH_4 + H$. Curves ν_1–ν_3 are the nondegenerate a_1 modes and curves ν_4–ν_7 are the degenerate e modes. Imaginary frequencies are plotted as negative numbers in this figure.

$\Delta H_{298}°$ for the reaction, and the calculated saddle-point barrier height without (V^*) and with (ΔV^{*G}) the inclusion of zero-point effects. As discussed above, the STO-3G barrier is too high, and this makes the imaginary frequency at the saddle point too high as well.

The projected[3,11c,16e] matrix of second derivatives at every third point was diagonalized to give the harmonic frequencies $\nu_n(s)$ and the corresponding generalized normal modes $L_{\alpha,\gamma,n,m_n}(s)$, where $\gamma = x, y, z$ and $n = 1$–7 ($n = 8$ refers to the imaginary frequency of the MEP; see Table IIIb). The variation of the frequencies along the reaction path is shown in Figure 14. The MEP consists primarily of the relative translational motion of methyl and molecular hydrogen in the reactant region and of methane and H in the product region. The diabatic mode correlating with ν_1 at the reactants, where it is the H–H stretch, with the antisymmetric motion indicated in Figure 15e at the transition state, and with ν_2 at products, where it is a C–H stretch, is the frequency that changes most appreciably. The remaining two modes with a_1 symmetry at the saddle point are ν_1 and ν_3. ν_3 is the deformation of methyl in the reactant region and the deformation of methane in the product region and overall shows little change along the reaction path. The motions corresponding to ν_1 and ν_3 at the saddle point are shown in parts f and g of Figures 15, respectively.

The three highest frequency modes of e symmetry, ν_4–ν_6, corresponding to the motions indicated in parts a–c of Figure 15, respectively, show very little change along the reaction path. The lowest frequency e mode, ν_7, is the torsion mode, i.e., the out-of-plane motion of the odd hydrogen (see Figure 15d), and ν_7 has become imaginary, which implies that the second derivative matrix has a second negative eigenvalue and the reaction path bifurcates. This means that the picture of a multidimensional harmonic well perpendicular to the reaction path is not valid beyond this point, and so, anharmonicity would be required for accurate calculations. In the present case, the zero-point energy of this mode was set equal to zero when the frequency became imaginary.

The harmonic frequencies shown can be compared to results obtained from ab initio calculations with a split-valence 4-31G basis by Yamashita and Yamabe,[30] as well as with calculations performed with analytic representations of the potential energy surface.[20] One of the differences between the frequencies shown here and those of Yamashita and Yamabe is the behavior of the two highest frequency modes of a_1 symmetry, ν_1 and ν_2. We have labeled all generalized transition-state modes adiabatically, and therefore, our results show an avoided crossing of ν_1 and ν_2. Yamashita and Yamabe, on the other hand, show a "nonadiabatic" representation of the modes.

The nonadiabatic coupling of vibrational coordinates due to curvature of the reaction is represented in the coupling elements

(26) Colwell, S. M. *Mol. Phys.* **1984**, *51*, 1217.
(27) Truhlar, D. G.; Kuppermann, A. *Chem. Phys. Lett.* **1971**, *9*, 269.
(28) (a) Schatz, G. C.; Walch, S. D.; Wagner, A. F. *J. Chem. Phys.* **1980**, *73*, 4536. (b) Schatz, G. C.; Wagner, A. F.; Dunning, T. H., Jr. *J. Phys. Chem.* **1984**, *88*, 221.
(29) *JANAF Theormochemical Tables, 2nd ed.*; Stull, D. R., Prophet, H., Eds.; National Standard Reference Data Series 37; U.S. NBS: Washington, DC, 1971.
(30) Yamashita, K.; Yamabe, T. *Int. J. Quantum Chem., Quantum Chem. Symp.* **1983**, *No. 17*, 177.

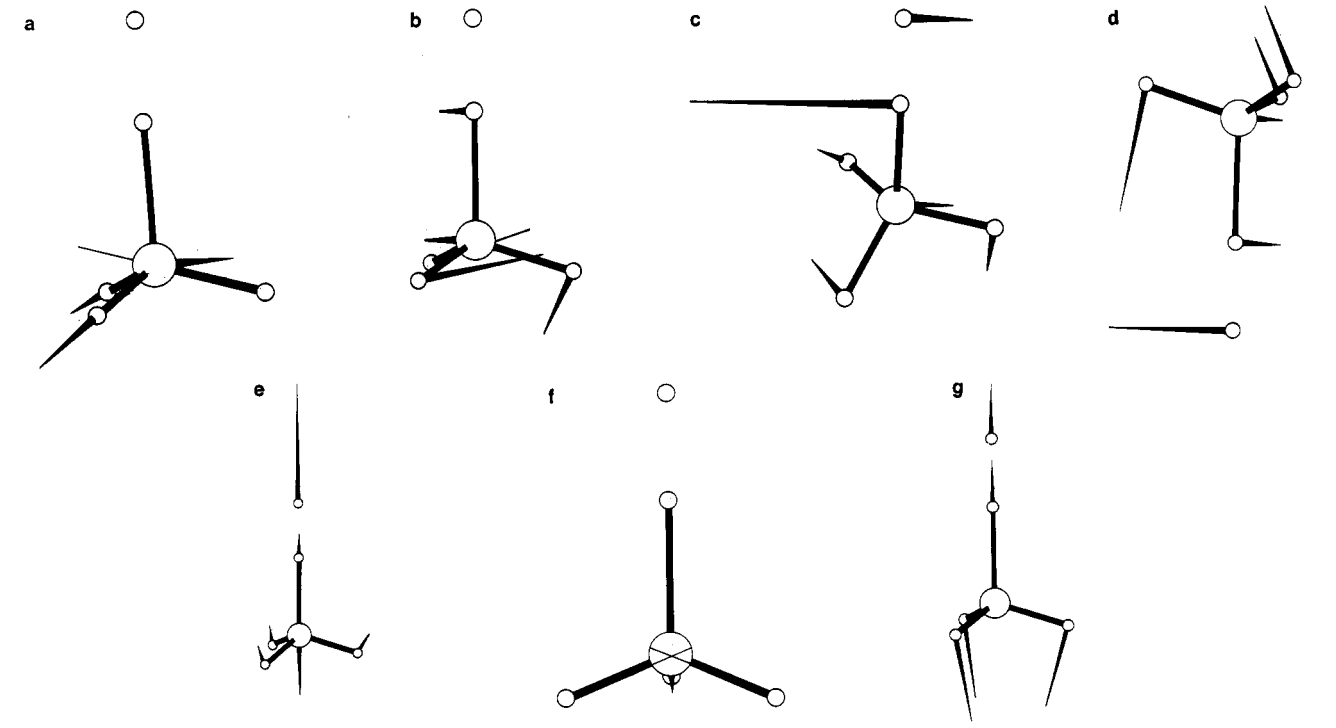

Figure 15. UHF/STO-3G normal mode ν_n of the CH_5 transition-state structure (C_{3v}) and the corresponding real frequency: (a) ν_4, 3794 cm^{-1}; (b) ν_5, 1773 cm^{-1}; (c) ν_6, 1550 cm^{-1}; (d) ν_7, 721 cm^{-1}; (e) ν_2, 1810 cm^{-1}; (f) ν_1, 3566 cm^{-1}; (g) ν_3, 1445 cm^{-1}.

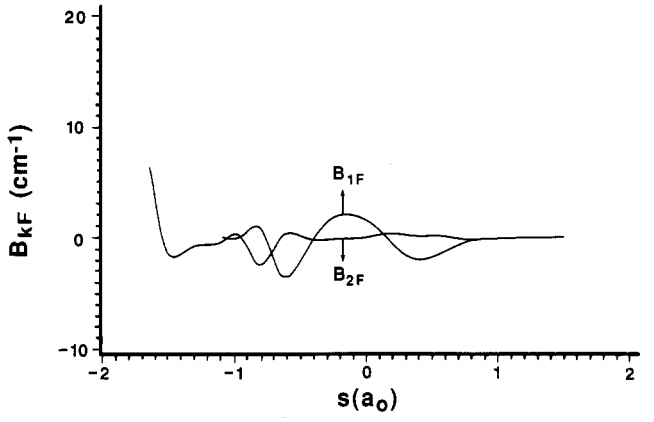

Figure 16. Curvature elements $B_{kF}(s)$, for $k = 1$ and 2, as a function of reaction coordinate s.

TABLE IV: Transmission Coefficients for the Reaction $CH_3 + H_2 \rightarrow CH_4 + H$

temp, K	$\ddagger/W$	CVT/MEPSAG	CVT/SCSAG
298	8.29	1.86×10^2	2.99×10^3
400	5.50	1.23×10^1	3.91×10^1
667	2.46	2.29	3.06
1000	1.65	1.44	1.62
1550	1.27	1.16	1.22

$B_{kF}(s)$, which arise from the curving of the MEP into the various generalized normal mode directions. Figure 16 shows the two of these coupling elements that change most significantly as a function of the distance measured along the MEP. The ν_1 and ν_2 modes, which change the frequency significantly as the reactive bond changes from an H_2 stretch in the reactant region to a CH stretch in the product region, show significant coupling to the reaction path.

The curvature of the reaction path is partitioned among the different vibrational modes as in eq 12; two components are illustrated in Figure 16. The curvature of the MEP has the effect of allowing corner-cutting tunneling,[3,11,17,21,31] thereby lowering

(31) Marcus, R. A.; Coltrin, M. E. *J. Chem. Phys.* **1977**, *67*, 2609.

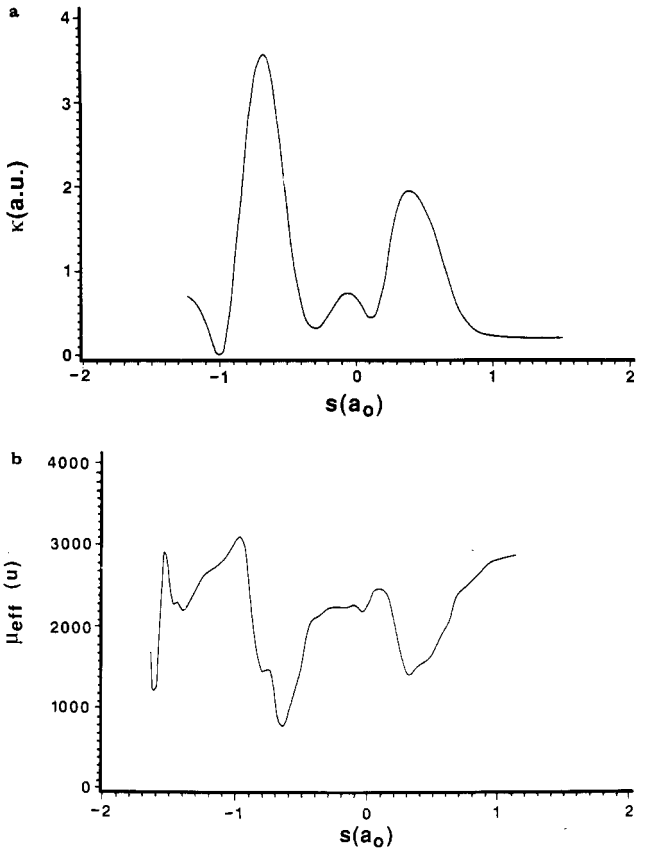

Figure 17. (a) Total curvature of the reaction path as a function of reaction coordinate. (b) Effective mass as a function of the reaction coordinate s.

the effective mass for the s motion. In this way, curvature increases the probability of tunneling through the barrier. Figure 17a shows the curvature of the reaction path. There are two sharp peaks, one before and one after the saddle point ($s = 0$), due to strong coupling with the H–H and C–H stretch modes, respectively. The very large peak on the reactant side in addition to

TABLE V: Forward Rate Coefficients (cm^3/(molecule s))

T, K	TST (‡)	ICVT/MEPSAG[a]	ICVT/SCSAG[a]	expt[b]
298	3.9×10^{-35}	7.3×10^{-33}	1.2×10^{-31}	...
400	6.5×10^{-30}	8.0×10^{-29}	2.5×10^{-28}	6.5×10^{-18}[b]
667	7.7×10^{-24}	1.8×10^{-23}	2.4×10^{-23}	9.0×10^{-16}[b]
1000	9.3×10^{-21}	1.3×10^{-20}	1.5×10^{-20}	1.5×10^{-14}[c]
1550	1.9×10^{-18}	2.2×10^{-18}	2.3×10^{-18}	...

[a] ICVT/MEPSAG agrees with CVT/MEPSAG, and ICVT/SCSAG agrees with CVT/SCSAG, to the number of significant figures shown. [b] Calculated from the reverse rate constants of Shaw and JANAF equilibrium constants.[29,33] [c] Calculated from the reverse rate constant of Sepehard et al. and JANAF equilibrium constants.[29,34]

these two peaks is due to the avoided crossing of ν_1 and ν_2 noted earlier; this large peak was not calculated in ref 7 because the avoided crossing was not resolved. (Another difference from ref 30 is that in the present work the curvature maximum at positive s is about 3 times larger than the one at $s \cong -0.1a_0$, whereas in their work the ratio of peak heights is about 1.3.) Figure 17b shows the effective mass as a function of reaction-path distance. This is one of the most difficult properties of the reaction path to converge, as is apparent from the extreme jaggedness of the plot, and as we know from many calculations[4,11,17,21] with analytic potential energy surfaces. (Fairly sharp peaks in the reaction path curvature as a function of the reaction coordinate are not uncommon; see, e.g., previous work on $H + H_2$[17] and $O + H_2$.[32]) The effective mass represents a consequence of the trends depicted in the curvature plot (Figure 17a) plus the distances to the vibrational turning points.

The rate constants were computed by both canonical-ensemble variational theory (CVT) and improved CVT (ICVT).[11,21] The canonical variational transition-state rate constant, k^{CVT}, can be formulated in terms of the generalized free energy of activation, as given by

$$k^{CVT}(T) = (\sigma/\beta h)K^\circ \exp\{-\max_s \Delta G^{GT,\circ}(T, s)/RT\} \quad (13)$$

where $\Delta G^{GT,\circ}(T, s)$ is the generalized transition-state standard-state free energy of activation at temperature T for a generalized transition state dividing surface at s, σ is the symmetry number, and K° is the reciprocal of the standard-state concentration. The ICVT rate constant[11c,21c] includes, in addition, a threshold correction.

Figure 18 shows plots of the generalized free energy of activation curves $\Delta G^{GT,\circ}(T, s)$ as functions of distance s along the reaction coordinate for four temperatures. For low temperatures, the maximum in the free energy profile occurs at $s = 0$, which corresponds to the saddle point. At higher temperatures, the maximum is just removed from $s = 0$. The effect is very small due to the fact that the STO-3G barrier height is so high. The free energy involves an enthalpy and an entropy contribution, and the zero-point effects or the other vibrational contributions in the latter often have the effect of moving the generalized transition state away from the saddle point. Since the potential energy term is so high for the UHF/STO-3G level of approximation, the vibrational effects on the location of the best transition state are relatively underestimated.

The Wigner approximation is the simplest tunneling correction to conventional TST. In addition to the information needed for conventional transition-state theory calculations, it is only necessary to know the imaginary frequency for the unbound normal mode at the saddle point. Table IV gives the Wigner tunneling approximation, $\ddagger/W$ (where $\ddagger$ refers to conventional TST), as a function of temperature. Since the restrictions involved in this approximation are so severe, the Wigner correction is justifiable only for reactions for which the variational transition state is located at $s = 0$ and even then only at very high temperatures where the value is near unity. When it differs appreciably from unity, as seen in Table IV for temperatures below 1000 K, the assumptions contained in its derivation are never satisfied and it is often found to be inaccurate.[21]

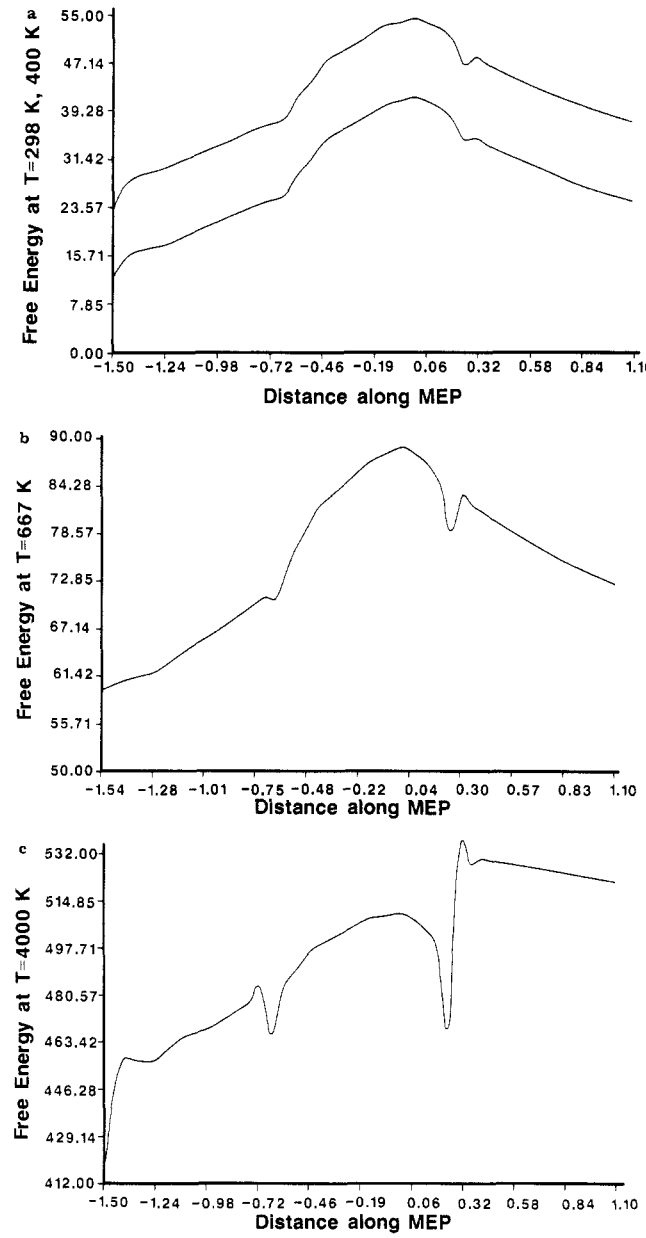

Figure 18. Generalized standard-state free energy of activation (kcal/mol) as a function of reaction coordinate for the temperatures (a) 298 and 400 K, (b) 667 K, and (c) 4000 K.

The calculation of more accurate transmission coefficients also corrects the VTST results somewhat for nonseparability of the reaction coordinate. Here, tunneling corrections are computed by the MEPSAG and SCSAG methods.[11,17,21] The latter approximation is the more accurate of the two, since it incorporates effects of the curvature of the reaction path. In those cases where there is no coupling of the reaction coordinate to the transverse vibrational modes in the tunneling region, MEPSAG should be a sufficient approximation to the transmission probability, but this is seldom the case. The more accurate SCSAG results are

(32) Garrett, B. C.; Truhlar, D. G. *Int. J. Quantum Chem.* **1986**, *29*, 1463.

also given in Table IV. At low temperatures, there is a 1 order of magnitude difference between the MEPSAG and SCSAG results, indicating the importance of reaction path curvature effects. At higher temperatures, where curvature has a smaller effect, the three sets of results merge to similar values. The transmission coefficients at the UHF/STO-3G level are expected to be too large because the barrier is too high and too thin.

The final rate constant is the product of $k^{CVT}(T)$ and $\kappa^{CVT/SCSAG}(T)$. Table V gives various approximations to the rate constants for (R1) as functions of temperature. Calculations performed with conventional TST without allowance for tunneling or curvature are given in the column headed with ‡. The final rate constants of this study are those in the column headed ICVT/SCSAG. As previously mentioned, the actual value of the rate constant is unreliable for (R1) because of the quality of the basis set. The forward rate constant is far too small compared to experiment[33,34] because of the overprediction of the barrier. It is still interesting to compare results obtained with various approximations, however, if we consider the present study to be a model of some other reaction with a higher barrier.

Allowance of tunneling but no curvature gives rate constants designated by ICVT/MEPSAG in Table V. These calculations ignore all reaction-path-curvature elements, but include the tunneling by the MEPSAG method, and this is appreciable at low temperatures. The inclusion of curvature effects yields even larger increases at low temperatures, as seen in the ICVT/SCSAG results. As the temperature increases, the two sets of tunneling results become almost identical, but at low temperatures there is as much as a 1-order of magnitude difference, as seen above in $\kappa(T)$.

The variation in the rate constant for the three methods without tunneling, ‡, CVT, and ICVT, is not significant for this model system until very high temperatures ($T > 1550$ K) are reached. It is only at these high temperatures that the no-recrossing assumption of conventional TST breaks down significantly more than that of VTST for the present model reaction.

(33) Shaw, R. *J. Phys. Chem. Ref. Data* **1978**, *7*, 1179.
(34) Sepehrad, A.; Marshall, R. M.; Purnell, H. *J. Chem. Soc., Faraday Trans. 1* **1979**, *75*, 835.

5. Summary and Conclusions

The efficiency of several methods for computing steepest descent paths has been compared. Euler, stabilized Euler, and a fourth-order Runge–Kutta method are shown to perform well.

A complete quantum mechanical calculation has been performed for the abstraction reaction (R1). The reaction path was generated by the stabilized Euler algorithm (version ES2) with step size $0.05a_0$, and generalized normal coordinates orthogonal to the path and vibrational frequencies were determined. This information has enabled calculation of the temperature-dependent rate constants with ab initio electronic structure calculations and the POLYRATE computer code without performing an analytic fit to the potential surface, i.e., "direct dynamics". The results include the effects of both tunneling and reaction path curvature.

The calculations show that it is possible to use electronic structure reaction path methods to study the dynamics of fairly large systems. (Of course "fairly large" is a relative descriptor; the present system has eleven vibrational degrees of freedom orthogonal to the reaction path, compared to two or three for an atom–diatom collision.) With the UHF/STO-3G level employed here, though, the results are not as accurate as previous results[20b] for reaction R1 with a semiempirical analytic potential surface. Thus, they represent a model system. It would also be interesting to investigate this system at a much higher level of calculation. When the level of electronic structure theory is good enough to give a reliable barrier and reaction path, the approach described in this work may provide useful accuracy for applications requiring rate constants.[11,21]

Acknowledgment. We are grateful to Frank Brown and Bruce Garrett for their contribution to earlier stages of this project. The work reported here was supported in part by grants to M.S.G. from the Air Force Office of Scientific Research (87-0049) and the National Science Foundation (CHE86-40771) and to D.G.T. from the U.S. Department of Energy, Office of Basic Energy Sciences (DE-FG02-86ER13579). The calculations were performed on a VAX 8530 (provided by AFOSR Grant 86-0237) and a Micro VAX II (provided by NSF Grant CHE85-11697), as well as the North Dakota State University IBM 3081 computer.

Registry No. CH_3, 2229-07-4.